Electronic Supplementary Information for:

Crystallographic Characterization of the Metal–Organic Framework $Fe_2(bdp)_3$ upon Reductive Cation Insertion

Naomi Biggins,[a,c] Michael E. Ziebel,[a,c] Miguel I. Gonzalez,[a] and Jeffrey R. Long[a,b,c]

[a]Department of Chemistry, University of California, Berkeley, California 94720, United States
[b]Department of Chemical and Biomolecular Engineering, University of California, Berkeley, California 94720, United States
[c]Materials Sciences Division, Lawrence Berkeley National Laboratory, Berkeley, California, 94720, United States

Experimental Details

General Information. Unless specified otherwise, all manipulations were performed under an inert atmosphere with rigorous exclusion of oxygen and water, either in an argon-atmosphere glovebox or using Schlenk techniques. The solvents *N,N*-dimethylformamide (DMF) and tetrahydrofuran (THF) were dried using a commercial solvent purification system designed by JC Meyer Solvent Systems. All other solvents and reagents were obtained from commercial sources and used without further purification.

Synthesis of 1,4-benzenedi(4′-pyrazolyl) (H_2bdp). Two procedures were used for the synthesis of H_2bdp. H_2bdp used in the bulk synthesis of microcrystalline $Fe_2(bdp)_3$ samples for gas sorption measurements was prepared as previously reported.[1] This procedure consistently yielded tan powders which suggested the presence of a trace impurity. Attempts to synthesize single crystalline $Fe_2(bdp)_3$ using this material typically produced low-quality single crystals. Single crystals of higher crystallinity were obtained by using H_2bdp that was synthesized via a Suzuki-Miyaura coupling of 1,4-dibromobenzene and 1-(2-tetrahydropyranyl)-1*H*-pyrazole-4-boronic acid pinacol ester using conditions similar to those reported previously for the synthesis of H_2bdp analogues.[2] This procedure yielded white powders free of any trace impurities.

Synthesis of $Fe_2(bdp)_3$ single crystals. Single crystals of $Fe_2(bdp)_3$ of X-ray diffraction quality were prepared via an adaptation of the reported synthesis for microcrystalline $Fe_2(bdp)_3$ powder.[3] In air, a 0.5 in outer diameter borosilicate tube was charged with $Fe(acac)_3$ (151 mg, 428 mmol), H_2(bdp) (30.0 mg, 143 mmol), anhydrous DMF (2 mL) and 1 equiv. of acetylacetone (14 μl, 0.14 mmol) as a weakly acidic modulator. The reaction mixture was degassed via 3–5 freeze-pump-thaw cycles, after which the tube was flame-sealed and placed in an oven at room temperature. The reaction was heated to 150 °C at 1 °C/min, then held at this temperature for 50 h. After this time, the tube was removed from the oven and cooled to room temperature. The resulting crystals were transferred to a 20 mL vial in air. The solvent was decanted and replaced with fresh DMF (10 mL), and the crystals were allowed to soak for at least 6 h. This was repeated five more times until the supernatant was colorless. This washing procedure was repeated with dichloromethane (6 × 10 mL) and THF (6 × 10 mL). The crystals were then transferred to a Schlenk flask, washed with dry, degassed THF (6 × 10 mL) under an Ar atmosphere, and then transferred to an Ar-atmosphere glove box. To avoid cracking of the crystals, the crystals were stored under THF until they were used for chemical reductions or single crystal diffraction measurements.

Chemical reduction of single crystals. We chose to target the fully reduced frameworks $A_2Fe_2(bdp)_3$ (A = Li^+, Na^+, K^+) as the greater cation loading in these materials was predicted to facilitate the identification of the cation positions in the difference Fourier maps. Single crystals of reduced $Na_2Fe_2(bdp)_3{\cdot}y$THF and $K_2Fe_2(bdp)_3{\cdot}y$THF were made via a similar method to that reported for the reduction of microcrystalline $Fe_2(bdp)_3$.[4] Sodium and potassium naphthalenide solutions were prepared by stirring the alkali metal with a 10% molar excess of naphthalene in THF until all the metal had visibly reacted. The naphthalenide solutions were added dropwise to crystals suspended in THF in four aliquots over the course of 2 h. As the single crystals of $Fe_2(bdp)_3$ could not be completely dried for the reduction reactions, the mass of the framework used in each reaction was estimated by calculating the theoretical yield of $Fe_2(bdp)_3$ crystals from a single sealed tube and using the full quantity of single crystals from that reaction in the

subsequent reduction. Because of uncertainty in the exact mass of these crystals and the inability to completely dry the crystals prior to reduction (in addition to the slow diffusion of naphthalenide into the single crystals in the unstirred vial versus smaller powder crystallites, and the possibility of residual DMF and/or CH_2Cl_2 from incomplete solvent exchange), an excess (1.2 to 1.5 equiv relative to iron) of the alkali metal naphthalenide was used in the single crystal reductions. This excess was required to ensure a crystallographically characterizable level of reduction and cation loading close to the target reduction level. The resulting solutions were left to react for 1 to 2 months before activation or single crystal X-ray diffraction experiments.

Single crystals of $Li_2Fe_2(bdp)_3{\cdot}y$THF were prepared by an alternative method. A small number of crystals (~10 μg or less) were placed into a custom-made frit inside a 20 mL vial (Figure S2) containing 100 mg of $Fe_2(bdp)_3$ powder, a magnetic stir bar, and enough THF to cover the crystals in the frit. Reductions were carried out using a procedure similar to the one above, but the stoichiometry of the lithium naphthalenide was calculated based on the mass of the $Fe_2(bdp)_3$ powder and the desired reduction level. The reactions were left to stir for 2 to 4 weeks prior to activation or single crystal X-ray diffraction experiments.

Activation of reduced single crystals. Reduced single crystals of $A_2Fe_2(bdp)_3{\cdot}y$THF ($A = Li^+$, Na^+) were immersed in 10 mL of benzene inside of an argon glove box and left to soak for at least 6 h. This was repeated twice a day for one week to remove all traces of THF. After the final wash, the crystals were transferred to a Schlenk flask and the majority of the solvent was decanted. The flask was removed from the glovebox and transferred to a Schlenk line, frozen in a dry ice bath and left overnight under dynamic vacuum to sublime the benzene. Following this, the crystals were transferred back into the glovebox and coated in Paratone-N oil.

Chemical reduction of microcrystalline $Fe_2(bdp)_3$ powder to yield $A_xFe_2(bdp)_3$ ($A = Li^+$, Na^+, K^+). Microcrystalline $Fe_2(bdp)_3$ was synthesized according to the literature procedure.[4] Potassium, sodium, and lithium naphthalenide were prepared by stirring the corresponding alkali metal with a 10% molar excess of naphthalene in THF. Bulk reduction of $Fe_2(bdp)_3$ powder using the corresponding alkali metal naphthalenides was carried out following the reported procedure for the synthesis of $K_xFe_2(bdp)_3$.[4] The samples were collected by filtration and ICP-OES analysis was performed to determine the iron to alkali metal ratio.

Chemical reduction of powder $Fe_2(bdp)_3$ to yield $Mg_{0.85}Fe_2(bdp)_3$. Magnesium anthracene was prepared according to a literature procedure.[5] Activated, microcrystalline $Fe_2(bdp)_3$ (150 mg, 0.204 mmol) was suspended in 10 mL of THF and a stoichiometric amount of magnesium anthracene (85.3 mg, 204 mmol) was added in four portions over 2 h with magnetic stirring. The suspension was stirred for 12 h. The resulting dark brown/black powder was collected via filtration and soaked in 10 mL of benzene for 24 h to remove any traces of anthracene. The solvent was then decanted and replaced with fresh benzene. This procedure was repeated five more times, and the reduced product was collected by filtration and ICP-OES analysis was used to determine the Mg:Fe ratio.

Inductively coupled plasma optical emission spectroscopy. Inductively coupled plasma optical emission spectroscopy (ICP-OES) was performed on a Perkin Elmer Optima 7000 DV ICP-OES in the Department of Chemistry at the University of California, Berkeley. Powder samples (2–3 mg) were digested by stirring in ca. 2 mL of piranha solution at 60 °C until the frameworks dissolved, typically yielding pale-yellow solutions.

Single-crystal X-ray diffraction. X-ray diffraction data for $Fe_2(bdp)_3 \cdot x$DMF were collected at Beamline 11.3.1 at the Advanced Light Source, Lawrence Berkeley National Laboratory using synchrotron radiation (λ= 0.8856 Å), and data for the remaining structures were collected at Beamline 12.2.1, also at ALS (λ= 0.7288 Å) with a Bruker AXS D8 diffractometer equipped with a PHOTON II detector. The crystals were coated with Paratone-N oil and mounted on a MiTeGen loop, then cooled to 100 K using an Oxford Cryosystems cryostream for data collection. Raw data were integrated and corrected for Lorentz and polarization effects using Bruker AXS SAINT[6] software and corrected for absorption using SADABS.[7] Space group assignments were determined by examination systematic absences, E-statistics, and successive refinement of the structures. All structures were solved by intrinsic phasing using SHELXT.[8] Additional refinement was performed with SHELXL[9] operated within the OLEX2[10] interface. Thermal parameters were refined anisotropically for all non-hydrogen atoms. All hydrogen atoms were placed geometrically and refined using the riding model.

Refinement details for $Fe_2(bdp)_3 \cdot x$DMF. A DMF molecule was located within the framework pores and was disordered over two positions due to a two-fold axis parallel to the *c* axis and was modelled accordingly. Displacement parameter restraints (SIMU and RIGU), distance restraints (DFIX), and geometric constraints (FLAT) were necessary to model the solvent disorder. SIMU and RIGU were applied to the benzene rings of the organic linkers in order to achieve a stable refinement.

Refinement details for $K_2Fe_2(bdp)_3 \cdot y$THF. Disorder of the potassium cation required the use of displacement parameter restraints (SIMU and RIGU). A linear free variable restraint (SUMP) was used on the three-component cation disorder to restrain the sum of the occupation factors to unity. Displacement parameter restraints (SIMU and DELU) were applied to the benzene rings of the organic linkers in order to achieve a stable refinement.

Refinement details for solvated $Na_2Fe_2(bdp)_3 \cdot y$THF. Disorder of the sodium cation required the use of a displacement parameter restraint (SIMU). A linear free variable restraint (SUMP) was used on the three-component cation disorder to restrain the sum of the occupation factors to unity. A displacement parameter restraint (SIMU) was applied to the benzene rings of the organic linkers in order to achieve a stable refinement. Three instances of OMIT were used (OMIT 0 2 2, OMIT 0 4 4, OMIT 0 4 0). These reflections were suspected to be affected by the beamstop.

Refinement details for activated $Na_{0.5}Fe_2(bdp)_3$. Displacement parameter restraints (SIMU and DELU) were applied to the benzene rings of the organic linkers in order to achieve a stable refinement. Two instances of OMIT were used (OMIT 0 2 2, OMIT 0 0 4). These reflections were suspected to be affected by the beamstop. We note that PART 1 and PART 2 were applied to the two disordered Na atoms on special positions rather than PART -1 and PART -2 as instabilities in the refinement arose with the application of the negative PART functions (significant movement of the positions, growth in the ellipsoid sizes, and NPD atoms). We suspect this occurs because the application of negative PART functions to the single atoms removes the appropriate positional and U_{ij} special position constraints that SHELXL applied to these atoms, leading to instabilities in the refinement. In this case specifically, it is the removal of the U_{ij} constraints that gives rise to refinement issues.

Refinement details for activated $Li_2Fe_2(bdp)_3$. The occupancy of the lithium site refined to ~100%, thus the occupancy was fixed to be 1. Displacement parameter restraints (SIMU and DELU) were applied to the benzene rings of the organic linkers in order to achieve a stable refinement. Three instances of OMIT were used (OMIT 0 2 2, OMIT 0 0 4, OMIT 0 2 10). These reflections were suspected to be affected by the beamstop.

Discussion of cation occupancies in the single-crystal structures. As discussed in the main text, there is some intrinsic error and ambiguity in determining the cation occupancies in the solvated crystals. In the solvated structures ($K_2Fe_2(bdp)_3 \cdot y$THF and $Na_2Fe_2(bdp)_3 \cdot y$THF) it was not possible to unequivocally locate or refine any THF molecules in the electron density map. However, any solvent present in the pores is expected to be highly disordered and generate diffuse electron density that is unlikely to contribute significantly to the cation occupancies. This is supported by fact that the maximum values of the electron density in the final difference Fourier maps are low, which suggests that there is no significant electron density that has not been modelled. This is confirmed by the checkcif reports, which do not generate any high-level alerts relating to detectable, unmodelled electron density. As such, refined cation occupancies discussed here are unlikely to be heavily influenced by residual electron density from disordered THF.

While the presence of THF may slightly increase the refined occupancy of cations in the solvated structures, this difference alone is unlikely to fully explain the disparity in cation occupancy between the solvated and activated sodium-containing structures, which were taken from the same batch of reduced crystals. Variation in the cation occupancies between crystals could arise from a number of sources. For example, for the solvated crystals, the amount of THF in each crystal may be different. Additionally, because of the small mass of the crystals, the crystal reductions are highly sensitive to any residual DMF or CH_2Cl_2, which will react with the alkali naphthalenide reductant. Consequently, even small differences in the amount of residual reactive solvent from crystal to crystal could result in large differences in the extent of reduction. Furthermore, the crystals were not stirred during the reduction process to preserve their single-crystallinity and to ensure there were crystals large enough for diffraction. Because the naphthalenide reduction is likely diffusion-limited, the absence of stirring is likely to introduce some heterogeneity in the extent of crystal reduction. Differences in crystal size may further enhance heterogeneities introduced by slow diffusion of the reductant.

Powder X-ray diffraction (PXRD). Powder diffraction data for THF-solvated $Fe_2(bdp)_3$, $Li_{1.18}Fe_2(bdp)_3$, $Li_{1.90}Fe_2(bdp)_3$, $Na_{1.14}Fe_2(bdp)_3$ and $Na_{2.06}Fe_2(bdp)_3$ were collected with Cu Kα (λ = 1.5406 Å) radiation and 0.02° steps using a Bruker D8 Advance diffractometer. Synchrotron PXRD data for $Mg_{0.85}Fe_2(bdp)_3$ were collected at Beamline 17-BM-B (λ = 0.4522 Å) at the Advanced Photon Source at Argonne National Laboratory. All reduced samples were loaded into 1.0 mm borosilicate capillaries inside a nitrogen or argon atmosphere glovebox and flame-sealed before data collection.

For $Na_{1.14}Fe_2(bdp)_3$ and $Na_{2.06}Fe_2(bdp)_3$, a standard peak search, followed by indexing via a single value decomposition, as implemented by TOPAS-Academic v4.1,[11,12] enabled determination of approximate unit cell dimensions. Precise unit cell dimensions were obtained by performing a structureless Pawley refinement in TOPAS-Academic in order to obtain structural parameters that could be compared to the single-crystal data. Powder X-ray diffraction data for the sodium frameworks were collected after activation at 180 °C to show that the frameworks remain

crystalline after this treatment. The choice to use the sodium structures for these analyses was arbitrary and similar preservation of crystallinity and unit cell expansion are observed for the lithium and potassium powder samples.[13]

Thermogravimetric analysis. Thermogravimetric analyses were carried out at a ramp rate of 2 °C/min under a 25 mL/min N_2 flow with a TA Instruments TGA Q5000. Air-sensitive samples were loaded onto a pre-weighed Pt pan and suspended in hexanes in an Ar-atmosphere glovebox, then sealed in a 20 mL borosilicate vial. The suspension was removed from the box and frozen with liquid N_2 whilst still in the vial, then transferred to the instrument to protect the sample from oxygen and moisture during sample loading. Samples were heated to 50 °C at a rate of 2 °C/min and held at that temperature for 1 h to evaporate the hexanes prior to analysis. This procedure leads to a sharp mass loss at low temperatures and a step at 50 °C for all samples. The TGA data for $Na_{1.14}Fe_2(bdp)_3$ was used to estimate the quantity of THF present in the solvated frameworks, as illustrated in Figure S22.

Hirshfeld surface analysis. Hirshfeld surface analysis (HSA)[14] was carried out on the cations in the activated structures of $Na_{0.5}Fe_2(bdp)_3$ and $Li_2Fe_2(bdp)_3$ to help visualize the intermolecular interactions within the crystal structures, using the *CrystalExplorer* 17.5 software.[15] We examined the d_{norm} surfaces, which highlight close contacts as bright red spots.[16] It should be noted that d_{norm} is symmetric in d_i (distance from the surface to the nearest nucleus inside the surface) and d_e (distance from the surface to the nearest nucleus outside the surface), meaning any close contact will appear as two red regions on the surface. Furthermore, in order to work well, HSA must be carried out on structures that have been fully characterized, i.e. the location of solvent molecules must be determined. As this was not possible in the two reduced solvated structures ($K_2Fe_2(bdp)_3$ and $Na_2Fe_2(bdp)_3$), HSA was not performed on these structures. Additionally, the presence of disorder can lead to issues when calculating the Hirshfeld surface, so for $Na_{0.5}Fe_2(bdp)_3$ the analysis was performed separately on two possible 'ordered structures' where each possible cation position was assumed to have an occupancy of 100%. The disorder of the benzene rings was kept in the structures for the calculation for consistency as the cation–π interaction distances were determined from the average centroid calculated for the two orientations in the crystal structures. However, we do not anticipate this disorder to have a significant effect on the calculation given the relatively small changes in the carbon atom positions between the two disordered orientations.

Gas adsorption measurements. Volumetric gas adsorption isotherms of activated framework samples were collected at 77 and 87 K over pressures ranging from 0 to 1.2 bar using a Mirometrics ASAP 2420 or ASAP 2020 instrument. Samples were transferred under a dinitrogen or argon atmosphere to a preweighed analysis tube, which was capped with a Micrometrics *TranSeal*. All samples were evacuated at 180 °C under dynamic vacuum until an outgas rate of less than 2 μbar/min was achieved. The evacuated analysis tube containing the degassed sample was weighed again to determine the mass of the sample. The tube was then transferred to the analysis port of the gas adsorption instrument and the outgas rate was again confirmed to be less than 2 mTorr/min. For all isotherms, warm and cold free space correction measurements were performed using ultra-high purity He gas (UHP grade 99.999% purity); N_2 and H_2 isotherms at 77 K were measured in liquid nitrogen baths. H_2 isotherms at 87 K were measured in liquid argon baths. Oil-free vacuum pumps and oil-free pressure regulators were used for all measurements.

Adsorption isotherm fitting. Langmuir surface areas were determined from N_2 adsorption data at 77 K using Micromeritics software. The Langmuir equation was applied from P/P_0 values ranging from 0.05 to 0.3. Batch-to-batch variations in the surface area of the parent $Fe_2(bdp)_3$ framework exist; therefore, the surface areas of the cation-containing frameworks are compared to the appropriate starting material surface area in Table S5.

Single-component, low-pressure H_2 isotherms at 77 and 87 K were independently fit using a tri-site Langmuir equation (Equation S1), where n is the total amount of gas adsorbed (mmol/g), q_{sat} is the saturation loading at site A, B or C (mmol/g), b is the Langmuir parameter associated with site A, B or C (bar^{-1}), v is the Freundlich parameter (a constant), and P is the pressure (bar). b is defined as shown in Equation S2, where E is the site-specific isosteric heat of adsorption (kJ/mol), R is the ideal gas constant (J/mol·K), and T is the temperature in K. These parameters were determined by a least-squares fitting and are listed in Table S6. Attempts to fit the data using a dual-site Langmuir expression lead to poor fits, as evidenced by the R^2, overall sum of R^2 values, and visual inspection.

$$n = \frac{q_{sat,A} b_A P^{v_A}}{1 + b_A P^{v_A}} + \frac{q_{sat,B} b_B P^{v_B}}{1 + b_B P^{v_B}} + \frac{q_{sat,C} b_C P^{v_C}}{1 + b_C P^{v_C}} \quad \text{(S1)}$$

$$b = b_0 e^{\frac{-E}{RT}} \quad \text{(S2)}$$

Isosteric enthalpy of adsorption calculations. Using the Langmuir fits, the isosteric heat of adsorption, Q_{st}, for H_2 can be calculated as a function of n. Wolfram Mathematica software was used to interpolate a series of data points from the Langmuir fits to obtain exact pressures for specific loadings at 77 and 87 K. Q_{st} (kJ/mol) values were calculated from these data points as a function of loading using the Clausius-Clapeyron equation (Equation S3), where R is the ideal gas constant (J/mol·K), and P is the pressure at a given n at either T_2 (87 K) or T_1 (77 K).

$$Q_{st} = -\frac{R[\ln(P_{T_2}) - \ln(P_{T_1})]}{T_2^{-1} - T_1^{-1}} \quad \text{(S3)}$$

Mössbauer spectral measurements. The iron-57 Mössbauer spectrum of $Mg_{0.85}Fe_2(bdp)_3$ was obtained at 5 K with a constant acceleration spectrometer and a cobalt-57 rhodium source. Prior to data collection, the spectrometer was calibrated at 290 K with α-iron foil. The reported isomer shifts are relative to the α-iron foil. Samples were prepared and sealed inside an Ar-atmosphere glovebox and contained roughly 15 mg/cm^2 of sample (2.4 mg/cm^2 of iron) diluted in boron nitride. All spectra were fit with symmetric Lorentzian quadrupole doublets using the WMOSS Mössbauer Spectral Analysis Software.[17]

Supplementary Figures and Tables

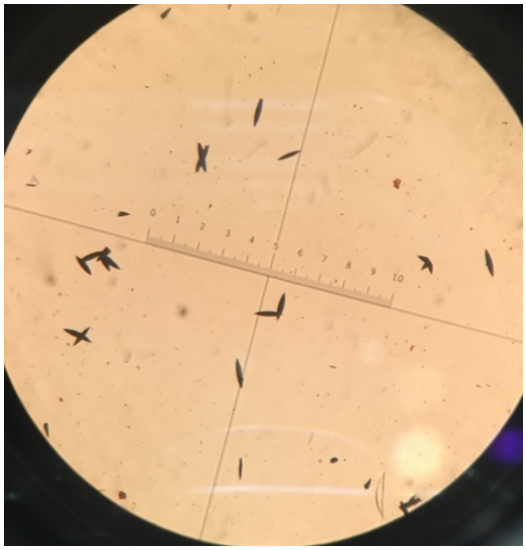

Figure S1. Photograph of single crystals of $Fe_2(bdp)_3 \cdot x$DMF.

Figure S2. Image of the custom-made frit used to house single crystals of $Fe_2(bdp)_3$ for stoichiometric reduction with lithium naphthalenide.

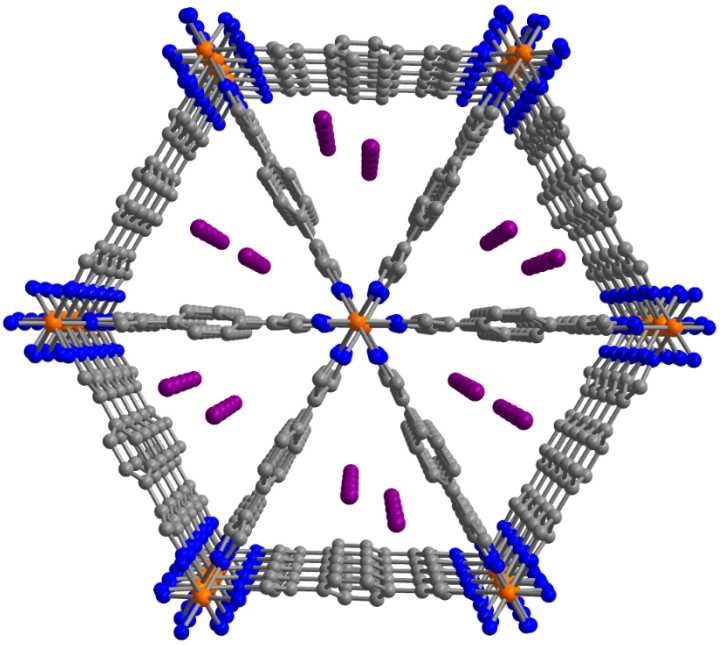

Figure S3. A portion of the single-crystal structure of activated $Na_{0.5}Fe_2(bdp)_3$. The two positions for the cation disorder are shown. Orange, purple, blue, and gray spheres represent Fe, Na, N, and C atoms, respectively; H atoms are omitted for clarity.

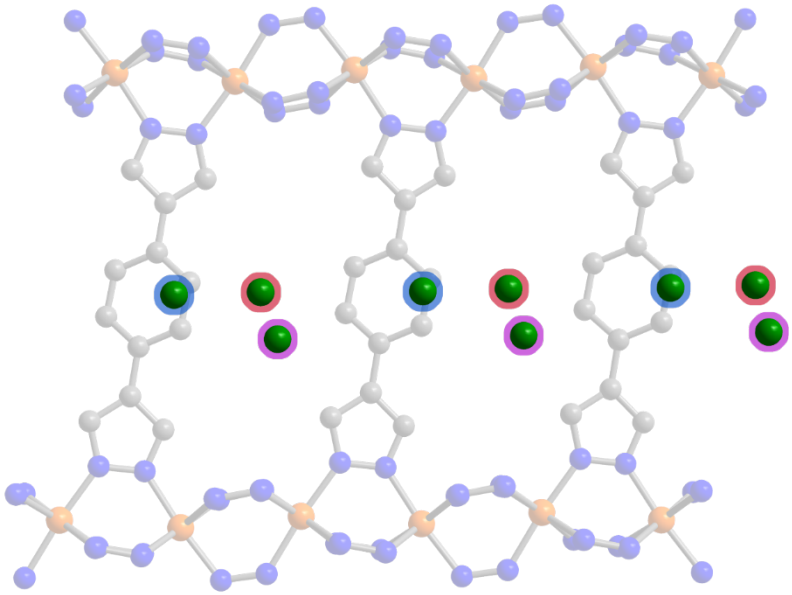

Figure S4. A view of the single-crystal structure of $K_2Fe_2(bdp)_3 \cdot y$THF in the *ac*-plane. Red, blue and purple circles around the potassium cations represent the different disorder sites. Orange, green, blue, and gray spheres represent Fe, K, N, and C atoms, respectively; H atoms are omitted for clarity, as are disordered K^+ sites generated by symmetry.

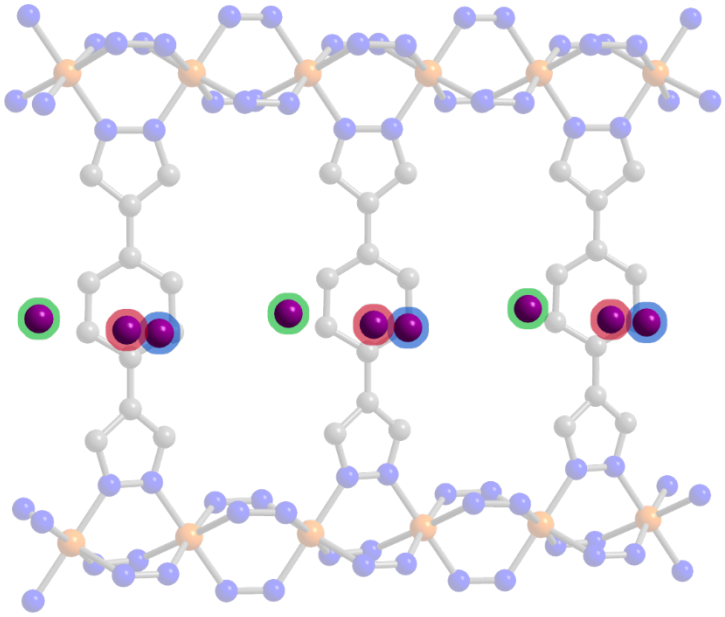

Figure S5. A view of the single-crystal structure of $Na_2Fe_2(bdp)_3 \cdot y$THF in the *ac*-plane. Red, blue and green circles around the sodium cations represent the different disorder sites. Orange, purple, blue, and gray spheres represent Fe, Na N, and C atoms, respectively; H atoms are omitted for clarity, as are disordered Na^+ sites generated by symmetry.

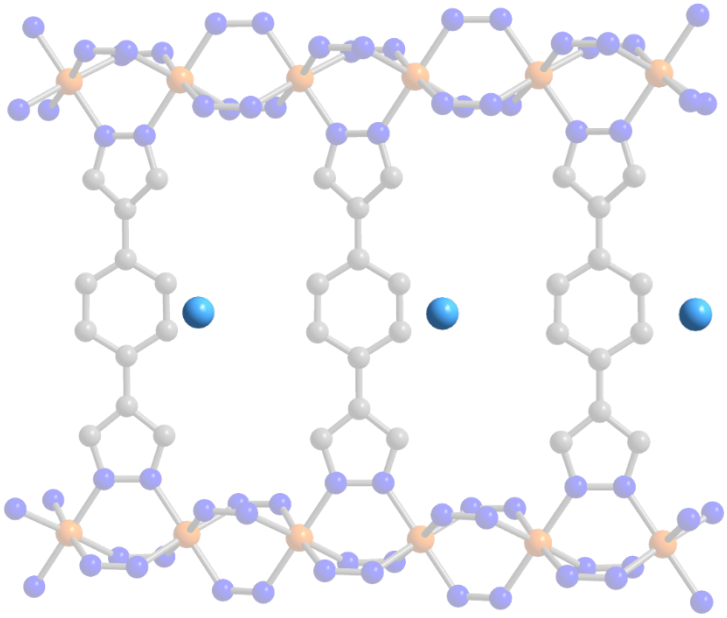

Figure S6. A view of the single-crystal structure of activated $Li_2Fe_2(bdp)_3$ in the *ac*-plane. Orange, light blue, blue, and gray spheres represent Fe, Li, N, and C atoms, respectively; H atoms are omitted for clarity.

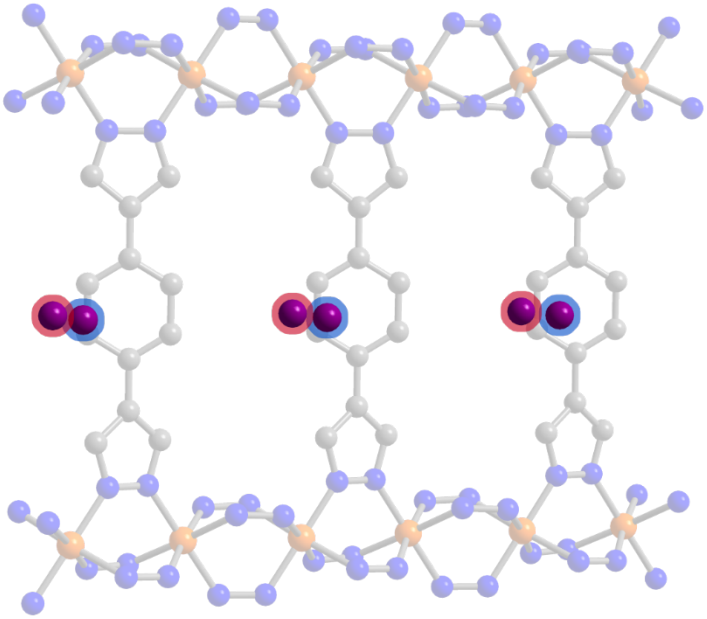

Figure S7. A view of the single-crystal structure of activated $Na_{0.5}Fe_2(bdp)_3$ in the *ac*-plane. Red and blue circles around the sodium cations represent the different disorder sites. Orange, purple, blue, and gray spheres represent Fe, Na, N, and C atoms, respectively; H atoms are omitted for clarity.

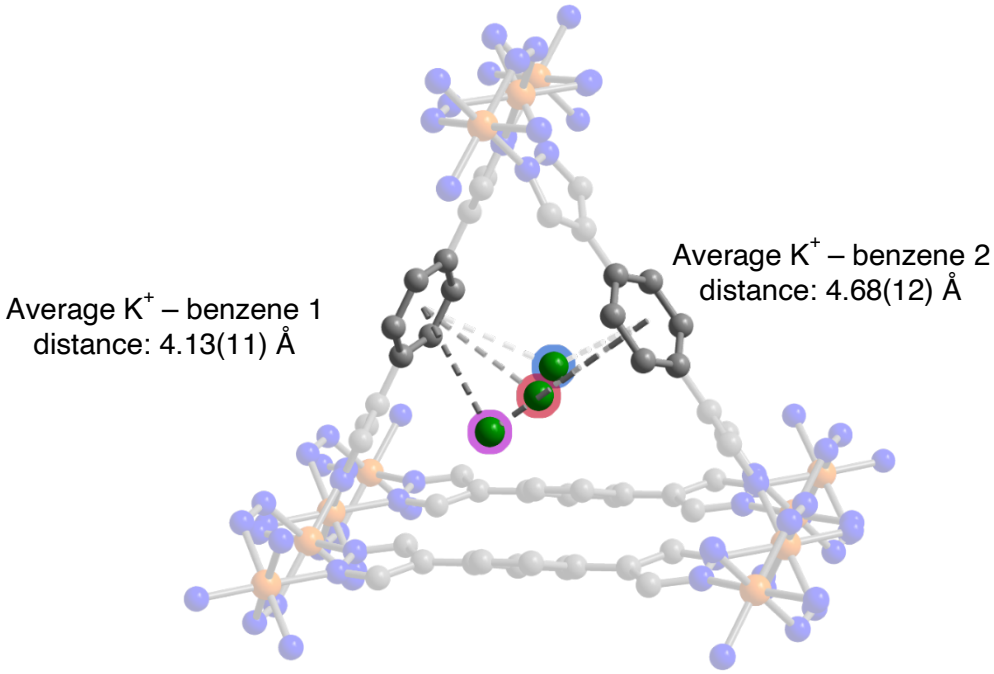

Figure S8. A portion of the single-crystal structure of $K_2Fe_2(bdp)_3 \cdot y$THF showing the interactions between the alkali cations and the benzene rings of the ligands. Red, blue and purple circles around the potassium cations represent the different disorder sites. Orange, green, blue, and gray spheres represent Fe, K, N, and C atoms, respectively; H atoms are omitted for clarity, as are disordered K^+ sites generated by symmetry.

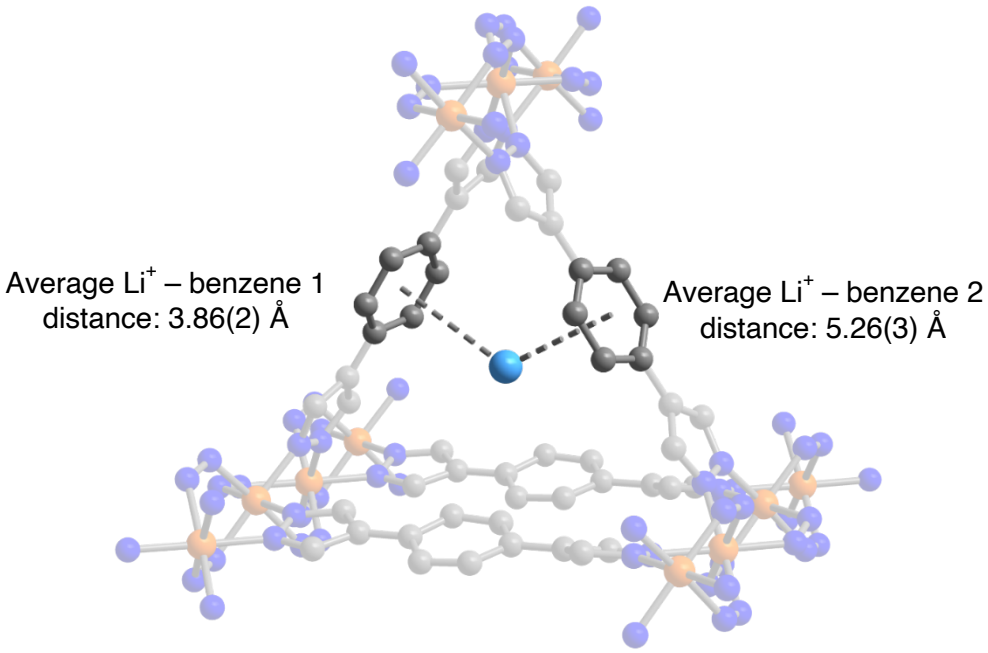

Figure S9. A portion of the single-crystal structure of activated $Li_2Fe_2(bdp)_3$ showing the interactions between the inserted cations and the benzene rings of the ligands. Orange, light blue, blue, and gray spheres represent Fe, Li, N, and C atoms, respectively; H atoms are omitted for clarity.

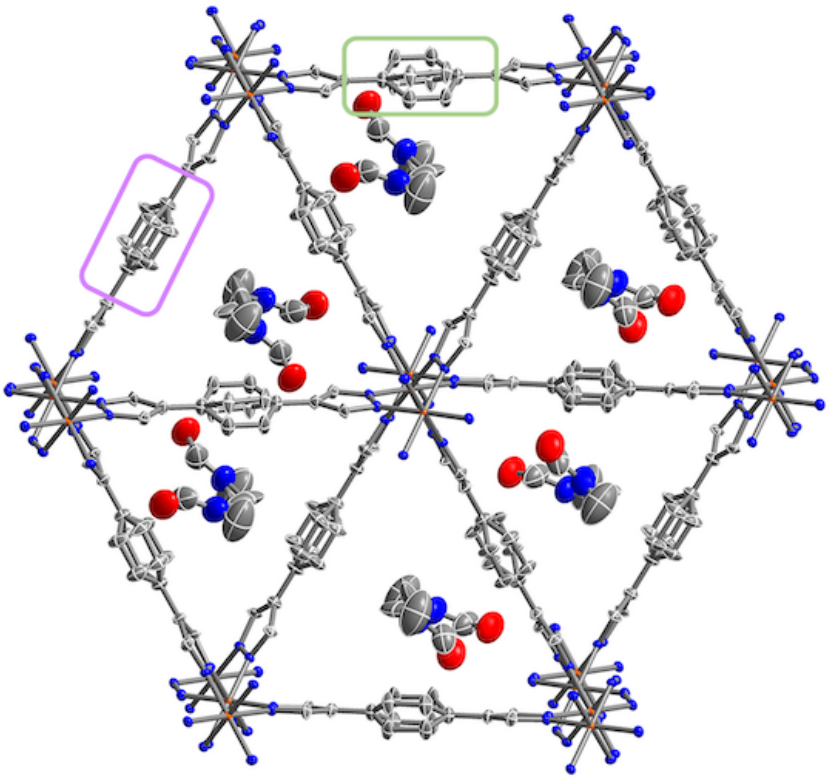

Figure S10. Atomic displacement parameter plot of DMF-solvated $Fe_2(bdp)_3$ at 100 K drawn at 50% probability level, showing the disorder of the DMF solvent molecule about a special position (2-fold rotation axis along *c*), as well as the disorder of the carbon atoms of the two crystallographically independent benzene rings (the ring highlighted in purple is made up of carbon atoms C4 and C5, which are disordered about an inversion center, and the green box highlights the disorder of the benzene ring containing carbon atoms C10–C13). It should be noted that type of disorder seen for the two benzene rings in this structure was seen in all structures reported in this work and has been modelled as such in all cases. Thus, the disorder of the benzene rings in this structure can be used to visualize the disorder of the benzene rings in the other structures. We note that the sizes of the thermal ellipsoids of the carbon atoms between structures varies slightly, so the anisotropic displacement parameters (ADPs) seen here should not be taken as being representative of the other structures. Information regarding the ADPs for the other structures can be found by examining the relevant .cif files. Orange, red, blue, and gray spheres represent Fe, O, N and C atoms, respectively; H atoms are omitted for clarity.

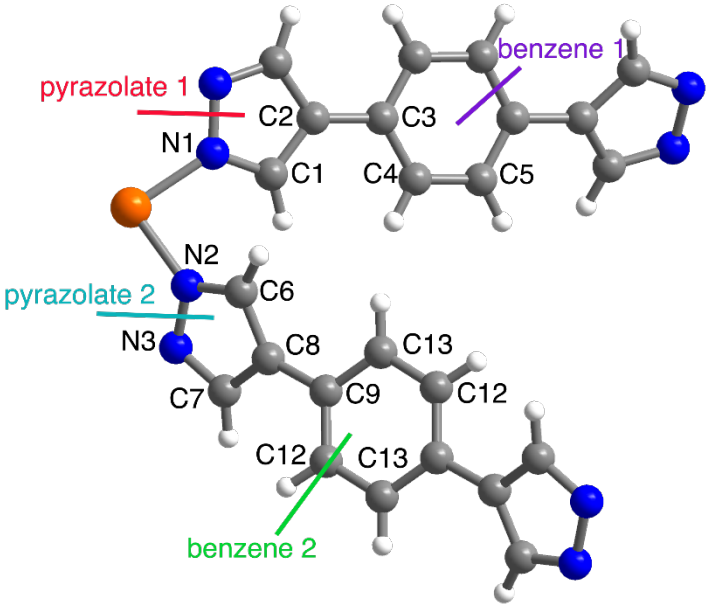

Figure S11. A general asymmetric unit for the $A_xFe_2(bdp)_3$ frameworks ($A = Li^+$, Na^+, K^+) with the atom numbering scheme shown in black and the benzene and pyrazolate labels shown in red, purple, turquoise and green. Note that only one part of the benzene disorder is shown for each ligand, and the missing atoms C10 and C11 correspond to carbon atoms that are part of one of the omitted disordered benzene rings.

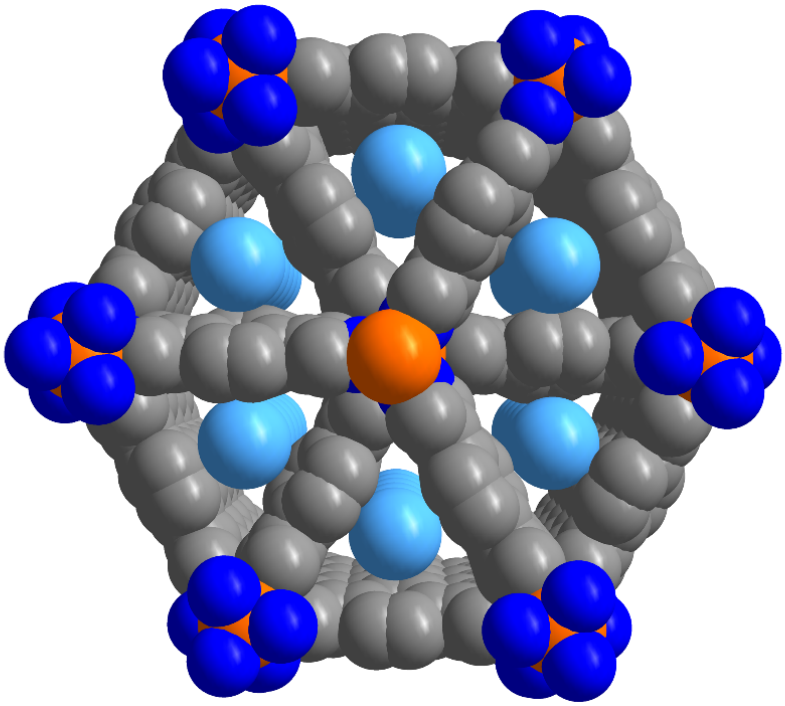

Figure S12. Space-filling model of activated $Li_2Fe_2(bdp)_3$.

Table S1. Crystallographic Data

	$Fe_2(bdp)_3$	$K_2Fe_2(bdp)_3$	$Na_2Fe_2(bdp)_3$	$Na_{0.5}Fe_2(bdp)_3$	$Li_2Fe_2(bdp)_3$
Formula	$C_{39.4}H_{32}Fe_2N_{13.1}O_{1.1}$	$C_{36}H_{24}Fe_2N_{12}K_{2.01}$	$C_{36}H_{24}Fe_2N_{12}Na_{2.04}$	$C_{36}H_{24}Fe_2N_{12}Na_{0.51}$	$C_{36}H_{24}Fe_2N_{12}Li_2$
Temperature (K)	100(2)	100(2)	100(2)	100(2)	100(2)
Crystal System	Orthorhombic	Orthorhombic	Orthorhombic	Orthorhombic	Orthorhombic
Space Group	*Fddd*	*Fddd*	*Fddd*	*Fddd*	*Fddd*
a, *b*, *c* (Å)	7.0648(4), 26.4382(14), 45.215(3)	7.081(3), 26.535(9), 45.388(19)	7.0835(3), 26.4668(12), 45.398(2)	7.0813(16), 26.493(7), 45.483(12)	7.0748(3), 26.4454(9), 45.3279(17)
α, β, γ (°)	90, 90, 90	90, 90, 90	90, 90, 90	90, 90, 90	90, 90, 90
V (Å^3)	8445.3(9)	8528(6)	8511.2(7)	8533(4)	8480(6)
Z	8	8	8	8	8
Radiation, λ (Å)	Synchrotron, 0.8856	Synchrotron, 0.7288	Synchrotron, 0.7288	Synchrotron, 0.7288	Synchrotron, 0.7288
2Θ Range for Data Collection (°)	4.448 to 61.962	3.646 to 57.99	3.68 to 54.19	6.167 to 62.62	6.182 to 52.076
Completeness to 2Θ	100% (2Θ = 61.962°)	100% (2Θ = 51.86°)	99.6% (2Θ = 51.86°)	99.9% (2Θ = 51.86°)	99.8% (2Θ = 51.86°)
Data / Restraints / Parameters	1749 / 106 / 189	2645 / 32 / 169	2180 / 19 / 169	3241 / 37 / 155	1957 / 37 / 149
Goodness of Fit on F^2	1.141	1.143	1.080	1.099	1.166
R_1[a], wR_2[b] ($I>2\sigma(I)$)	0.0718, 0.2025	0.0504, 0.1394	0.0568, 0.1618	0.0542, 0.1579	0.0599, 0.1766
R_1[a], $wR2$[b] (all data)	0.0857, 0.2123	0.0606, 0.1457	0.0713, 0.1747	0.0674, 0.1676	0.0731, 0.1918
R_{int}	0.0979	0.0801	0.1139	0.0888	0.1160
Largest Diff. Peak and Hole (e Å^{-3})	2.622 and –0.57	0.807 and –0.610	1.692 and –0.644	1.089 and –0.970	1.166 and –0.491

[a] $R_1 = \sum||F_o| - |F_c||/\sum|F_o|$. [b] $wR_2 = \{\sum[w(F_o^2 - F_c^2)^2]/\sum[w(F_o^2)^2]\}^{1/2}$.

Table S2. Unit cell dimensions for solvated crystals of $Fe_2(bdp)_3$ and $Na_2Fe_2(bdp)_3$ determined from single-crystal X-ray diffraction and solvated microcrystalline samples of $Fe_2(bdp)_3$, $Na_{1.14}Fe_2(bdp)_3$, and $Na_{2.06}Fe_2(bdp)_3$, determined from powder X-ray diffraction. All compounds crystallize in the space group *Fddd*. The dimensions for the powder samples are slightly larger than for the corresponding single-crystal samples as a result of the different data collection temperatures (298 versus 100 K, respectively).

	$Fe_2(bdp)_3$ single-crystal	**$Na_2Fe_2(bdp)_3$ single-crystal**	**$Fe_2(bdp)_3$ powder[18]**	**$Na_{1.14}Fe_2(bdp)_3$ powder**	**$Na_{2.06}Fe_2(bdp)_3$ powder**
a (Å)	7.0648(4)	7.0835(3)	7.1046(2)	7.0977(3)	7.1149(2)
b (Å)	26.4382(14)	26.4668(12)	26.4943(9)	26.2972(12)	26.598(9)
c (Å)	45.215(3)	45.398(2)	45.3489(9)	45.9384(3)	45.6537(13)
V (Å^3)	8445.3(9)	8511.1(7)	8356.1(4)	8574(7)	8640(5)

Table S3. Crystallographic occupancies and multiplicities of cations in solvated $A_2Fe_2(bdp)_3$ (A = Na^+, K^+) and activated $Na_{0.5}Fe_2(bpd)_3$. Wyckoff position 16g is a special position and directly corresponds to the chemical occupancy of the position. Wyckoff position 32h is a general position and the site occupancy of these positions needs to be doubled when calculating total chemical occupancy. Activated $Li_2Fe_2(bdp)_3$ is not included here as only one cation position was found, meaning the relationship between site and chemical occupancy[a] for the cation is direct.

Framework	Site occupancy of A^+1 (%), **Wyckoff position**	Site occupancy of A^+2 (%), **Wyckoff position**	Site occupancy of A^+3 (%), **Wyckoff position**	Total chemical occupancy (%)[b]
$K_2Fe_2(bdp)_3$	30.6, **32h**	14.0, **16g**	13.4, **32h**	102(2)
$Na_2Fe_2(bdp)_3$	25.3, **32h**	17.6, **32h**	17.2, **16g**	103(3)
$Na_{0.5}Fe_2(bdp)_3$	11.3, **16g**	13.3, **16g**	N/A	24.6(1.7)

[a]Site occupancy, which is equivalent to crystallographic occupancy, corresponds to the occupancy refined for the atom(s) in the asymmetric unit; it does not account for multiplicity. Chemical occupancy is with respect to the chemical formula and integrates the multiplicity of the crystallographic positions into its value.
[b]Note that in all cases, the Fe atom lies on special position 16g.

Table S4. A^+–centroid distances (in Å) in solvated $A_2Fe_2(bdp)_3$ (A = Na^+, K^+) and activated $Na_{0.5}Fe_2(bdp)_3$ for each of the disordered cation positions. The activated $Li_2Fe_2(bdp)_3$ structure is excluded from this table as there is only one cation position. The corresponding distances for the single Li^+ site can be found in Table 1. The error in the weighted average distances is largely derived from the error associated with the individual occupancies. See Figure S11 for a depiction of the asymmetric unit for all structures, illustrating the locations of the relevant pyrazolate and benzene rings.

Framework	Cation position	Cation occupancy	Benzene 1	Benzene 2	Pyrazolate 1	Pyrazolate 2
$K_2Fe_2(bdp)_3$	K1	30.6(8)	4.24(2)	4.069(19)	5.509(19)	5.62(2)
	K2	14.0(8)	3.883(9)	5.236(14)	5.607(6)	6.644(11)
	K3	13.4(6)	4.12(2)	5.501(19)	4.214(19)	6.701(19)
$Na_2Fe_2(bdp)_3$	Na1	25.3(9)	4.21(2)	4.659(18)	5.321(18)	5.711(18)
	Na2	17.6(8)	4.174(16)	4.823(15)	4.278(14)	6.43(14)
	Na3	17.2(11)	5.128(1)	3.949(11)	5.814(13)	6.552(8)
$Na_{0.5}Fe_2(bdp)_3$	Na1	11.3(15)	4.90(5)	4.13(4)	5.48(3)	6.38(4)
	Na2	13.3(9)	3.429(4)	6.760(16)	3.974(16)	6.41(16)

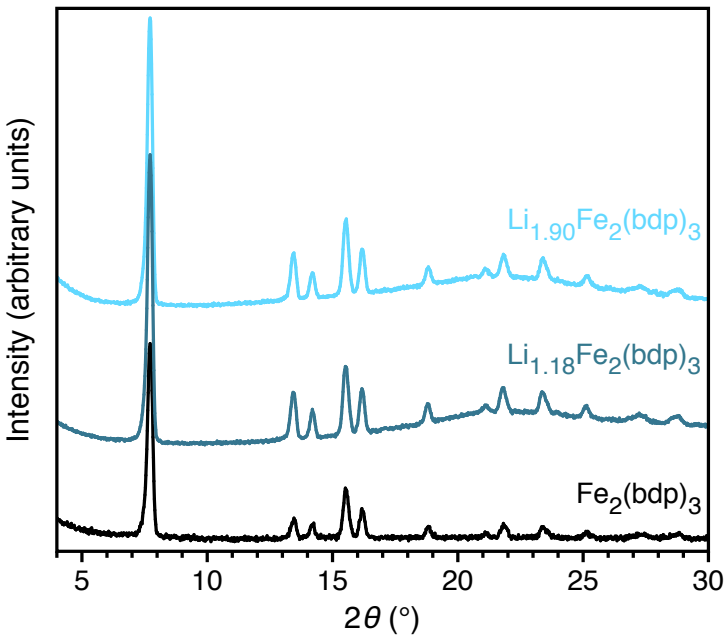

Figure S13. Room-temperature powder X-ray diffraction patterns of THF-solvated $Fe_2(bdp)_3$, $Li_{1.18}Fe_2(bdp)_3$, and $Li_{1.90}Fe_2(bdp)_3$ (λ = 1.5406 Å). The broad feature between 18–30° in the $Li_{1.18}Fe_2(bdp)_3$ and $Li_{1.90}Fe_2(bdp)_3$ data is background from a borosilicate capillary.

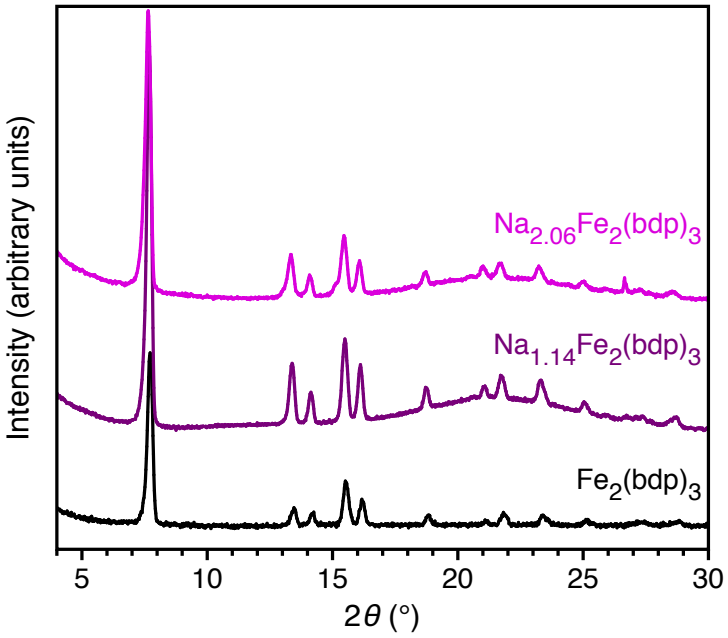

Figure S14. Powder X-ray diffraction patterns of THF-solvated $Fe_2(bdp)_3$, $Na_{1.14}Fe_2(bdp)_3$, and $Na_{2.06}Fe_2(bdp)_3$ (λ = 1.5406 Å). The broad feature between 18–30° in the data for $Na_{1.14}Fe_2(bdp)_3$ and $Na_{2.06}Fe_2(bdp)_3$ is background from a borosilicate capillary.

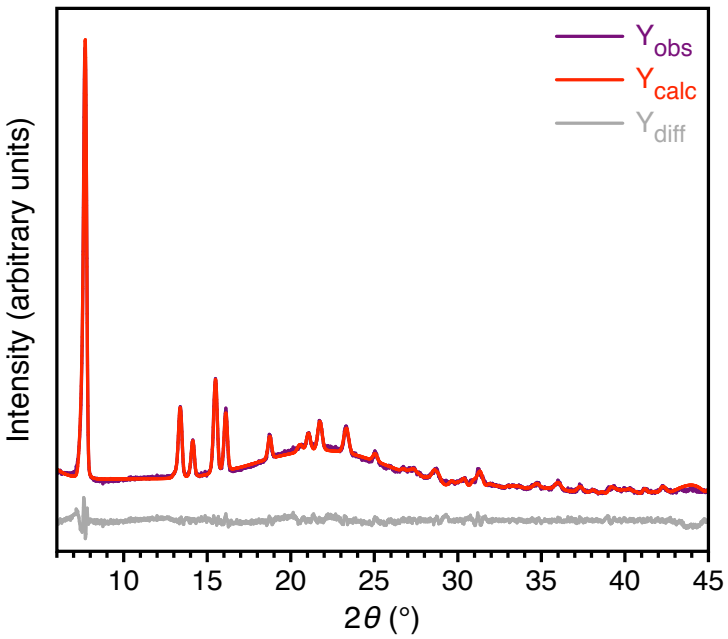

Figure S15. Pawley refinement for PXRD data of THF-solvated $Na_{1.14}Fe_2(bdp)_3$. Dark purple and red lines represent the observed and calculated diffraction patterns, respectively. The gray line represents the difference between the observed and calculated powder patterns. R_{wp} = 1.68%, GoF = 2.10%. The broad feature between ca. 18–30° is background from a borosilicate capillary.

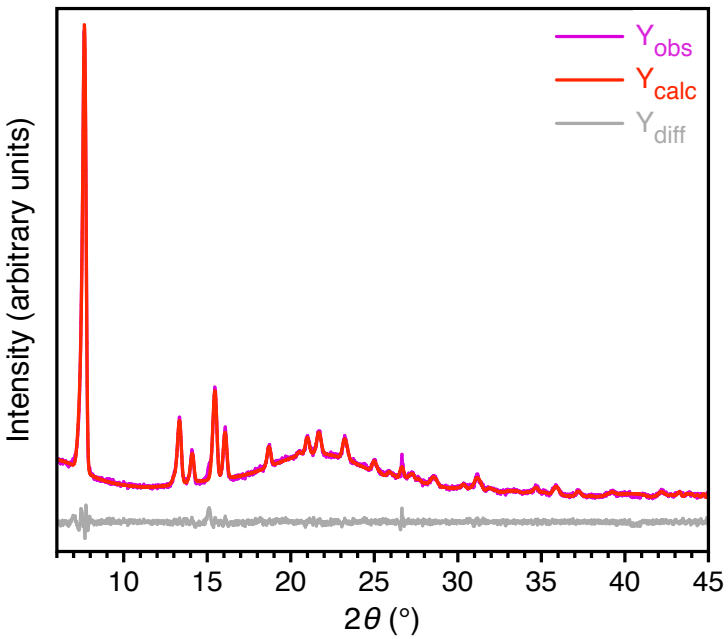

Figure S16. Pawley refinement of THF-solvated $Na_{2.06}Fe_2(bdp)_3$. Purple and red lines represent the observed and calculated diffraction patterns, respectively. The gray line represents the difference between the observed and calculated powder patterns. R_{wp} = 1.36%, GoF = 1.58%. The broad feature between ca. 18–30° is background from a borosilicate capillary.

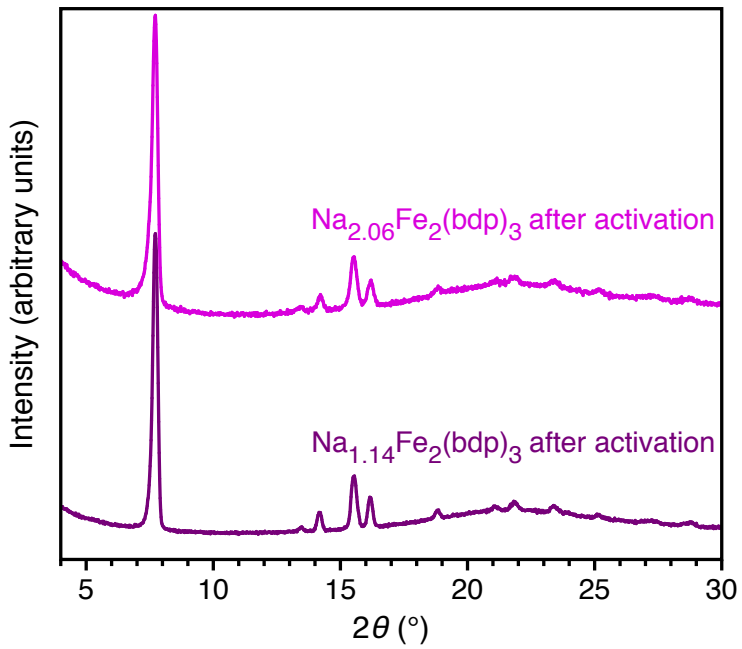

Figure S17. Powder X-ray diffraction patterns of the sodium reduced $Fe_2(bdp)_3$ frameworks after activation at 180 °C, collected at room temperature with λ = 1.54 Å (Cu radiation). The broad feature between ca. 18–30° is background from a borosilicate capillary.

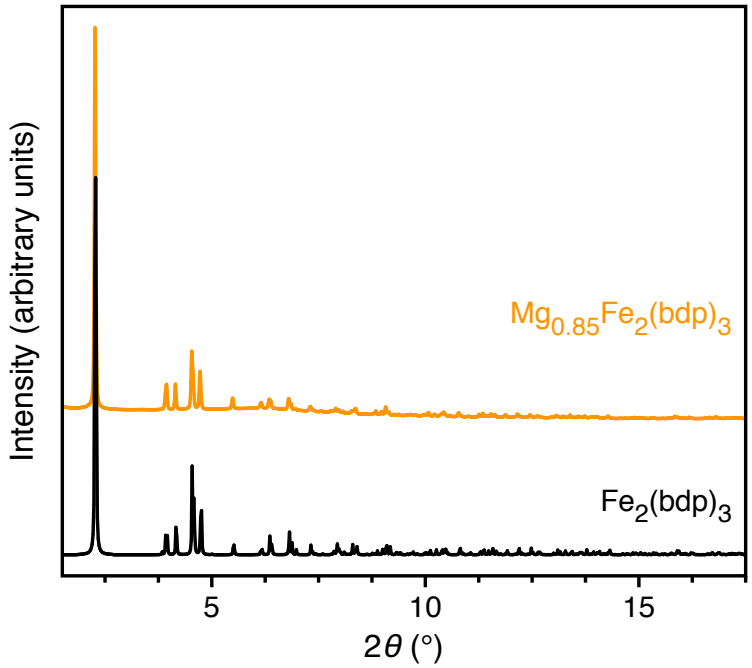

Figure S18. Powder X-ray diffraction pattern of solvated $Mg_{0.85}Fe_2(bdp)_3$, collected at room temperature with λ = 0.4522 Å. The diffraction pattern for $Fe_2(bdp)_3$ was calculated in Mercury from the single-crystal structure of the neutral framework.

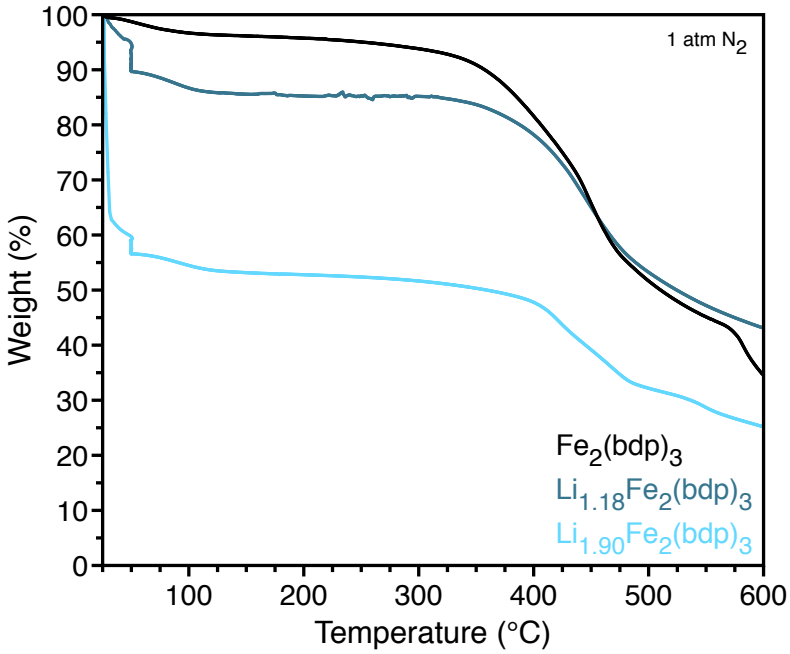

Figure S19. Thermogravimetric analysis data for THF-solvated $Fe_2(bdp)_3$, $Li_{1.18}Fe_2(bdp)_3$, and $Li_{1.90}Fe_2(bdp)_3$.

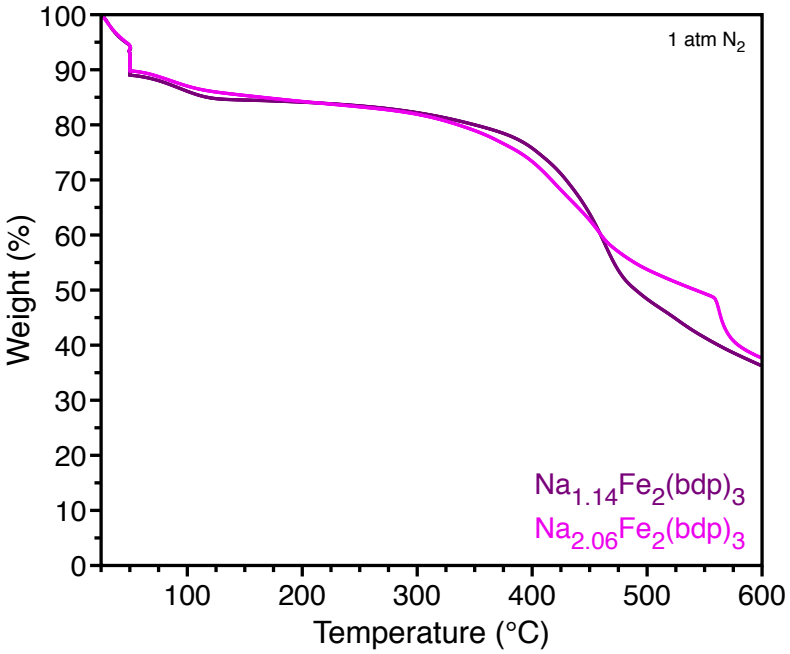

Figure S20. Thermogravimetric analysis data for THF-solvated $Na_{1.14}Fe_2(bdp)_3$ and $Na_{2.06}Fe_2(bdp)_3$.

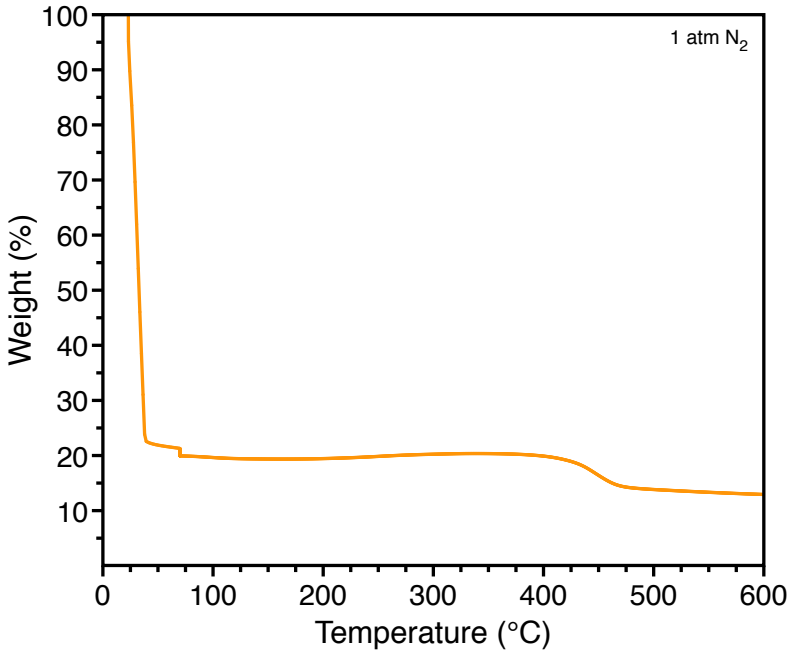

Figure S21. Thermogravimetric analysis data for $Mg_{0.85}Fe_2(bdp)_3$. The dramatic weight loss below 50 °C corresponds to loss of hexanes from the material.

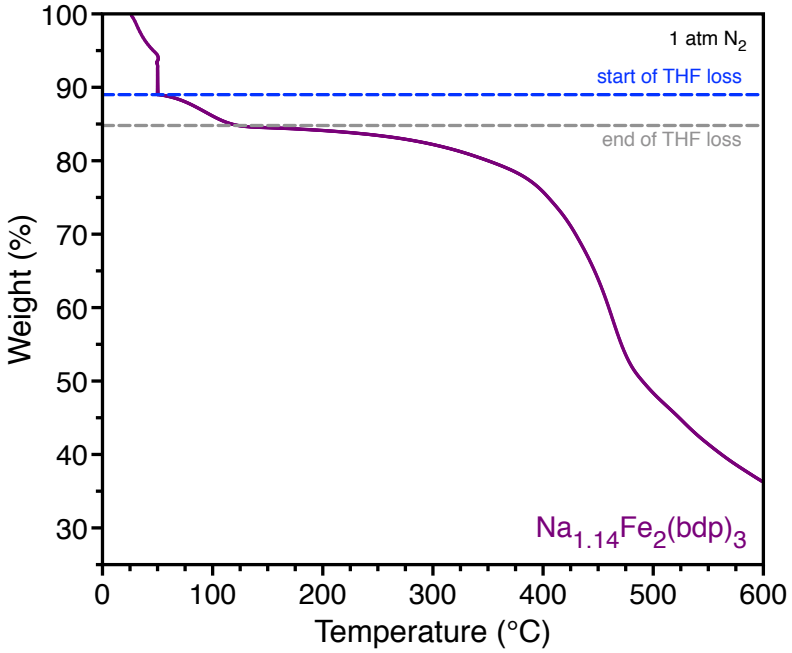

Figure S22. Thermogravimetric analysis data for microcrystalline, solvated $Na_{1.14}Fe_2(bdp)_3$, used as a representative example for the calculation of the quantity of THF present in the solvated frameworks. The blue and gray dashed lines correspond to the start and end of the weight loss regime that is attributed to removal of THF. For $Na_{1.14}Fe_2(bdp)_3$, the represented weight loss is 4.5%, which corresponds to a molecular weight of 34.32 g/mol. This equates to roughly half an equivalent of THF per molecular formula.

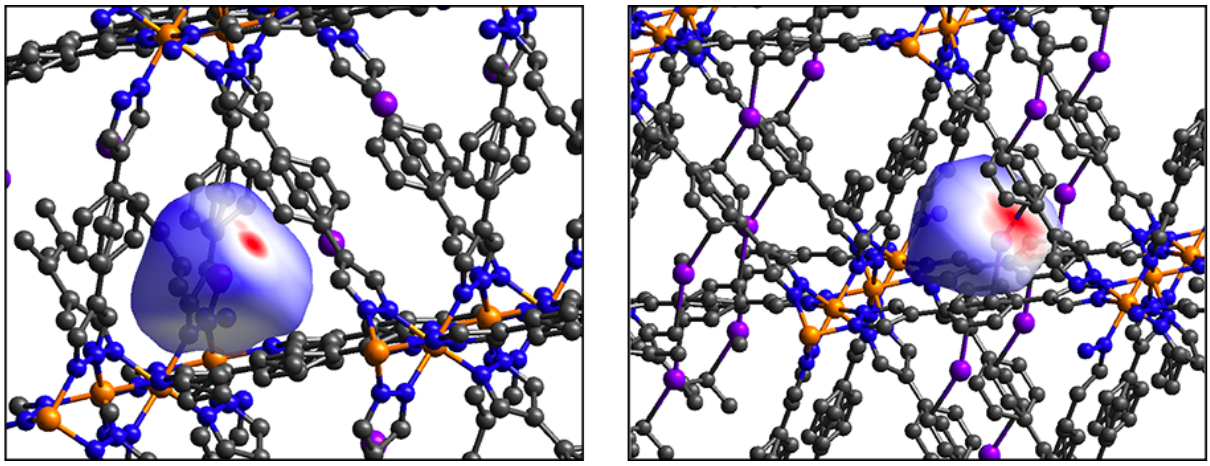

Figure S23. Hirshfeld surface of Na1 (left) and Na2 (right) in $Na_{0.5}Fe_2(bdp)_3$ mapped with d_{norm}. For this structure, the analysis was performed separately on the two disordered Na cation orientations to prevent the analysis from assigning interactions between the two cations. Because of the proximity of Na2 to one of the carbon atoms of one of the benzene rings, CrystalExplorer considers the two atoms to be 'bonded', but we note that this is not accurate and this bond should be ignored. It should be noted that the two red regions that appear in the surface for Na1 are a result of the symmetric nature of d_{norm}. Both Na cations show bright red spots in the direction of the nearest benzene rings, which is indicative of cation–π interactions. The red spot is larger on the surface of Na2 as this disordered position is closer to the benzene ring than Na1. Orange, purple, blue, and gray spheres represent Fe, Na, N, and C atoms, respectively; H atoms are omitted for clarity.

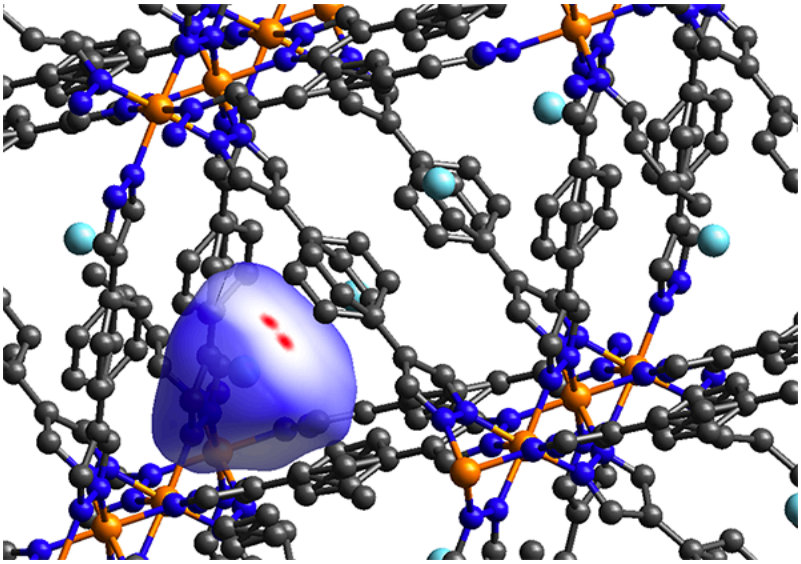

Figure S24. Hirshfeld surface of Li in $Li_2Fe_2(bdp)_3$ mapped with d_{norm}. Two red regions appear on the surface because of the symmetric nature of d_{norm}. The red spots are in the direction of the nearest benzene, which is indicative of cation–π interactions. Orange, light blue, blue, and gray spheres represent Fe, Li, N, and C atoms, respectively; H atoms are omitted for clarity.

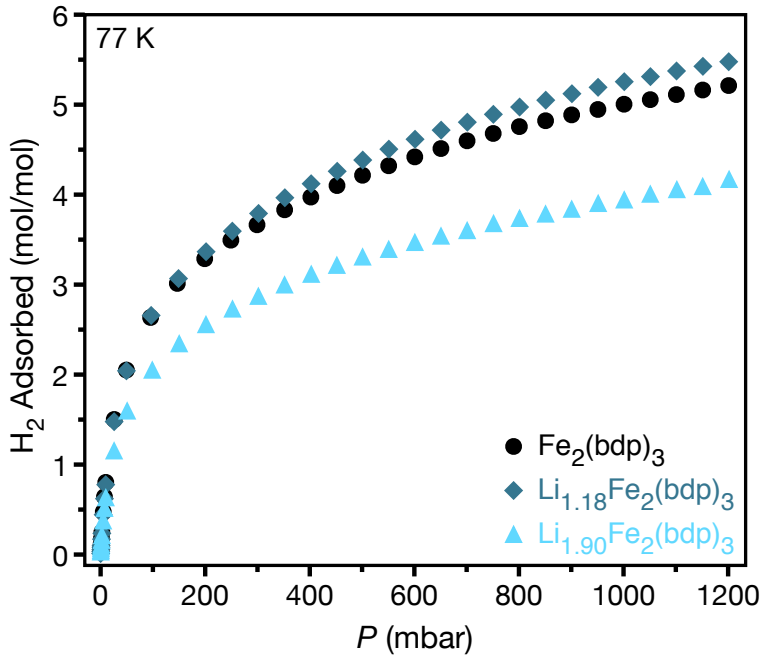

Figure S25. H_2 adsorption isotherms for activated $Fe_2(bdp)_3$, $Li_{1.18}Fe_2(bdp)_3$, and $Li_{1.90}Fe_2(bdp)_3$.

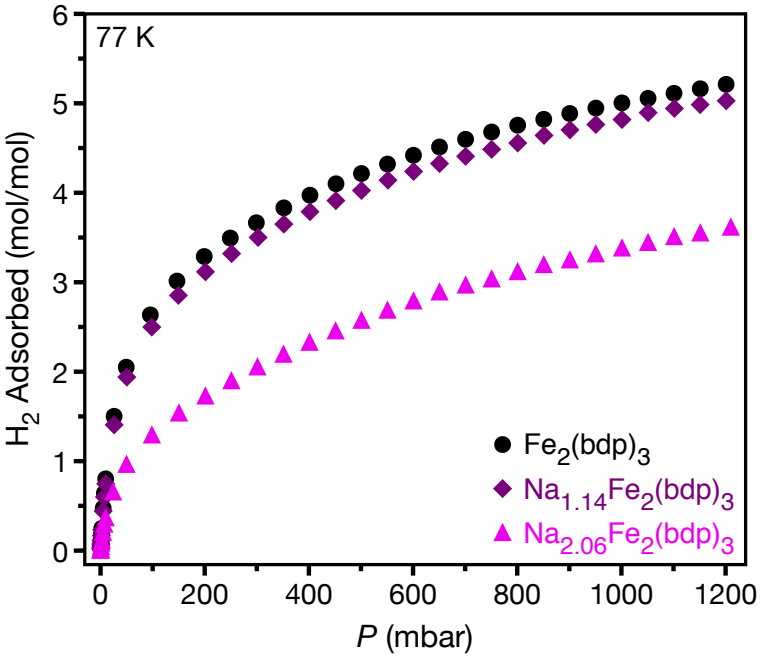

Figure S26. H_2 adsorption isotherms for activated $Fe_2(bdp)_3$, $Na_{1.14}Fe_2(bdp)_3$, and $Na_{2.06}Fe_2(bdp)_3$.

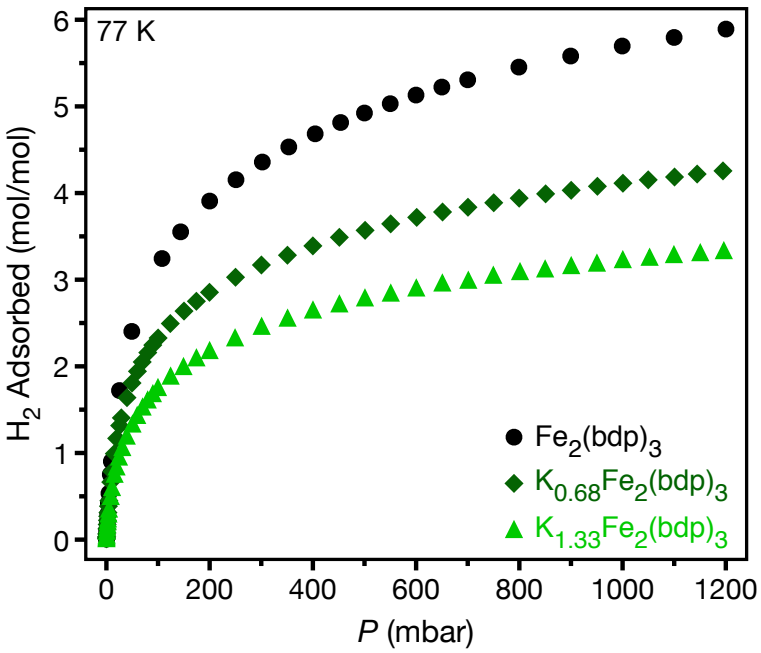

Figure S27. H_2 adsorption isotherms for activated $Fe_2(bdp)_3$, $K_{0.68}Fe_2(bdp)_3$, and $K_{1.33}Fe_2(bdp)_3$.

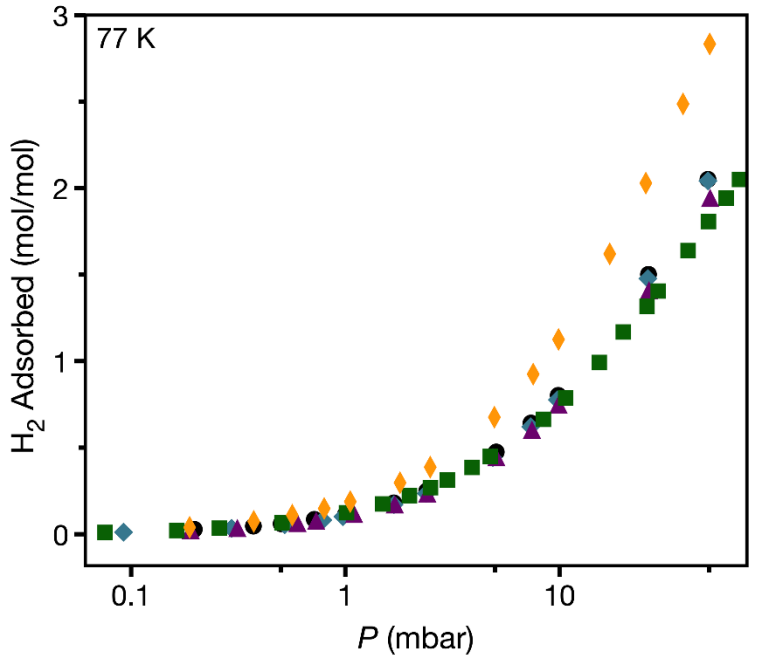

Figure S28. Expanded view of the low-pressure region for the plots in Fig. 4.

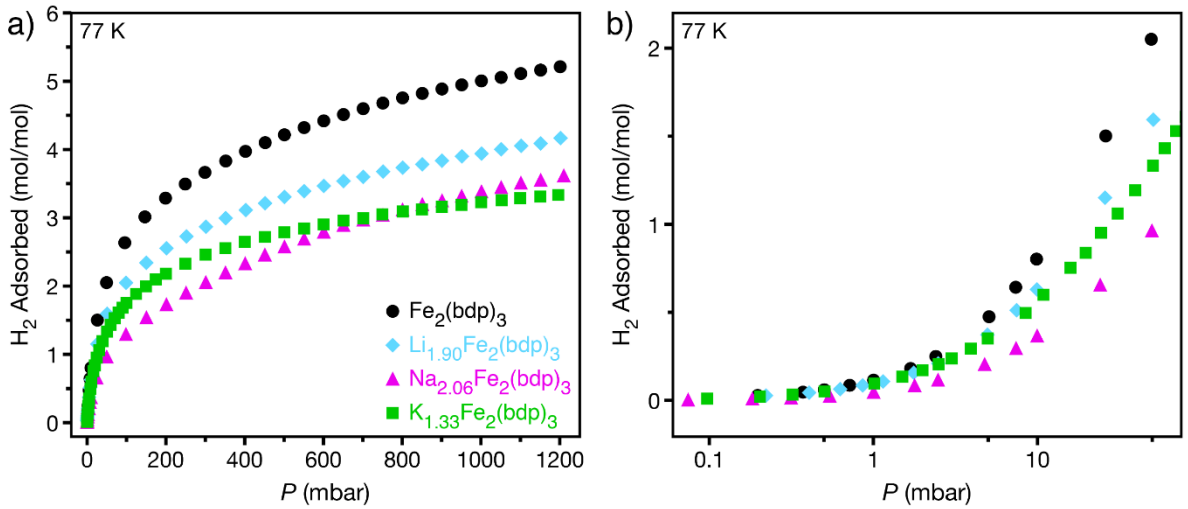

Figure S29. H_2 adsorption isotherms for activated microcrystalline powder samples of $Fe_2(bdp)_3$ and reduced variants at the highest cation loadings studied in this work. (b) Expanded view of the low-pressure region for all plots in (a).

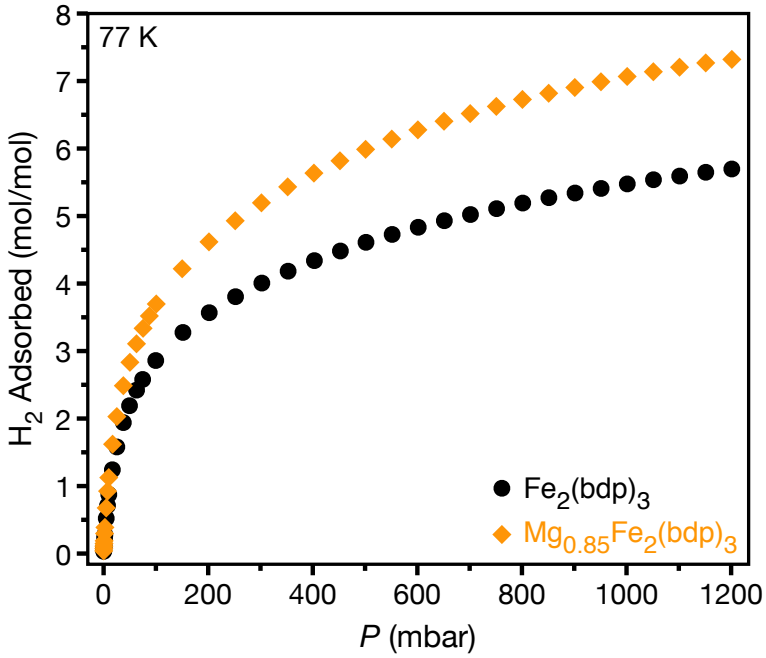

Figure S30. H_2 adsorption isotherms for activated $Fe_2(bdp)_3$ and $Mg_{0.85}Fe_2(bdp)_3$.

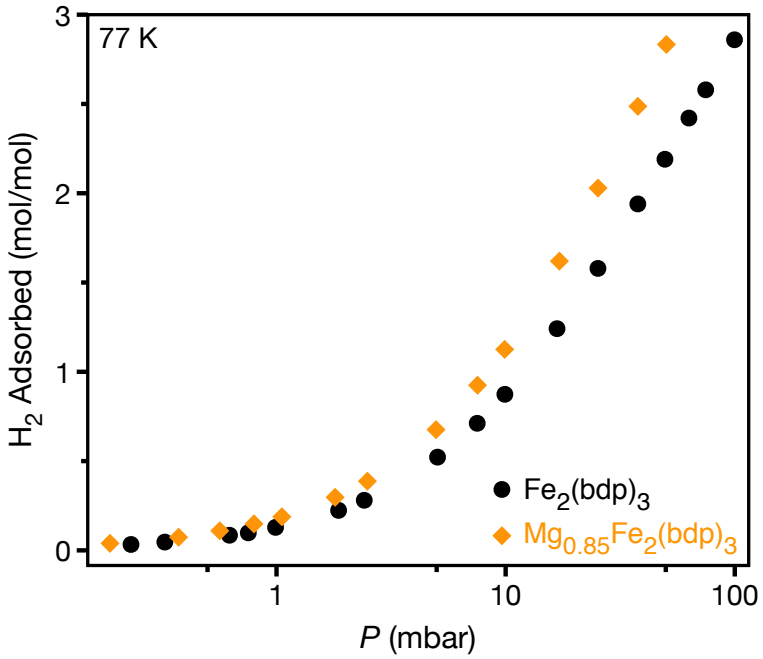

Figure S31. Expanded view of the low-pressure region of the H_2 adsorption isotherms for $Fe_2(bdp)_3$ and $Mg_{0.85}Fe_2(bdp)_3$.

Table S5. Surface areas for $A_xFe_2(bdp)_3$ ($A = Li^+, Na^+, K^+, Mg^{2+}$) determined from N_2 adsorption isotherms at 77 K. Variations in the calculated surface are for $Fe_2(bdp)_3$ arise due to defects, as has been reported previously.[4]

Langmuir surface area of $Fe_2(bdp)_3$ (m^2/g)	Reduced framework	Langmuir surface area (m^2/g)
783 ± 9	$Li_{1.18}Fe_2(bdp)_3$	772 ± 15
783 ± 9	$Li_{1.90}Fe_2(bdp)_3$	530 ± 6
783 ± 9	$Na_{1.14}Fe_2(bdp)_3$	643 ± 8
783 ± 9	$Na_{2.06}Fe_2(bdp)_3$	193 ± 8
923 ± 8	$K_{0.68}Fe_2(bdp)_3$	532 ± 6
923 ± 8	$K_{1.33}Fe_2(bdp)_3$	131 ± 1
928 ± 14	$Mg_{0.85}Fe_2(bdp)_3$	1028 ± 17[a]

[a] Increases in surface area following metalation have been reported previously, see ref. 19.

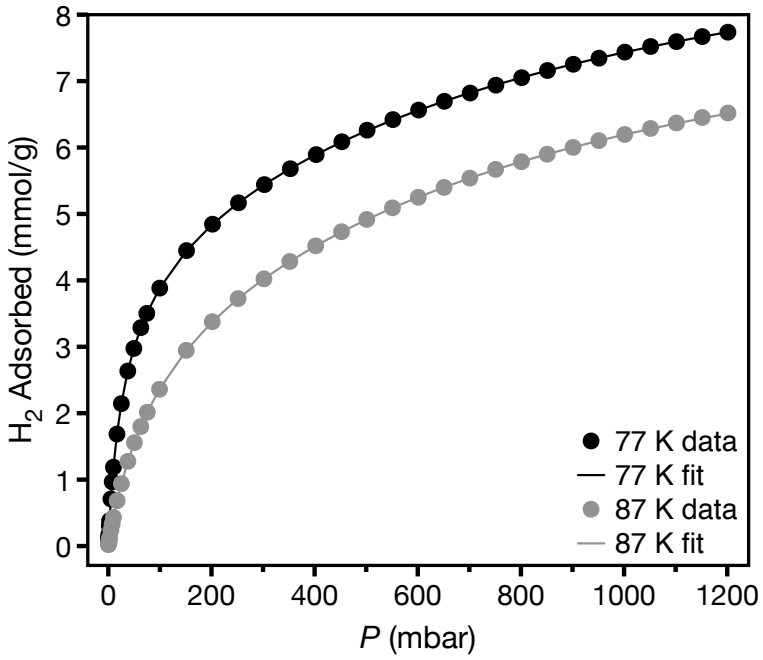

Figure S32. H_2 adsorption isotherms for $Fe_2(bdp)_3$ at 77 and 87 K (black and gray symbols, respectively) and their corresponding fits (lines).

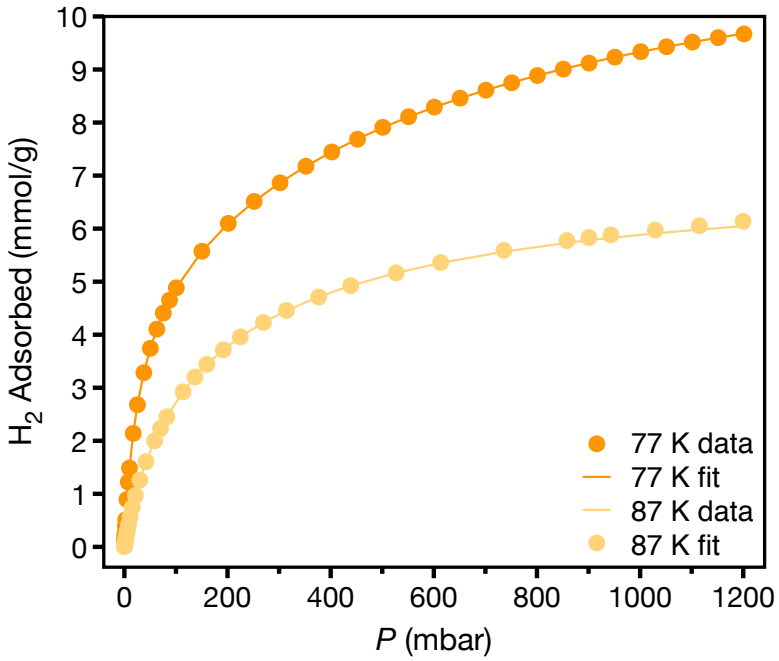

Figure S33. H_2 adsorption isotherms for $Mg_{0.85}Fe_2(bdp)_3$ obtained at 77 and 87 K (orange and yellow symbols, respectively) and their corresponding fits (lines).

Table S6. Tri-site Langmuir-Freundlich fit parameters obtained from fitting the H_2 adsorption isotherms of $Fe_2(bdp)_3$ and $Mg_{0.85}Fe_2(bdp)_3$.

	$Fe_2(bdp)_3$		$Mg_{0.85}Fe_2(bdp)_3$	
T (K)	77	87	77	87
$q_{sat,A}$ (mmol/g)	4.436	3.984	6.700	3.223
b_A (bar^{-1})	0.928	1.148	1.477	2.421
v_a	1.160	1.400	1.101	1.124
$q_{sat,B}$ (mmol/g)	4.204	1.055	2.911	0.926
b_B (bar^{-1})	27.729	11.558	30.086	22.648
v_B	0.942	1.067	1.052	1.484
$q_{sat,C}$ (mmol/g)	1.604	3.504	2.614	2.871
b_C (bar^{-1})	3.394	7.516	26.580	17.363
v_C	0.973	0.919	0.860	0.986

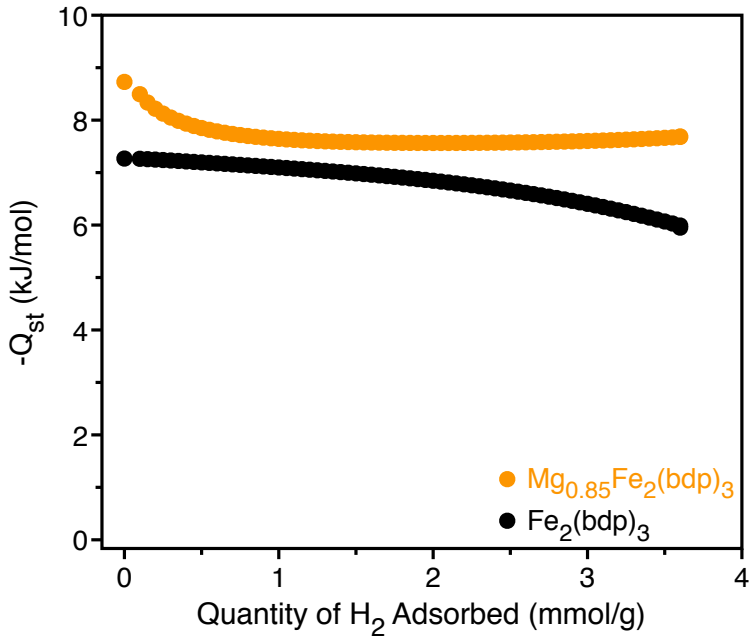

Figure S34. Isosteric heats of adsorption for $Fe_2(bdp)_3$ and $Mg_{0.85}Fe_2(bdp)_3$ plotted as a function of the amount of H_2 adsorbed.

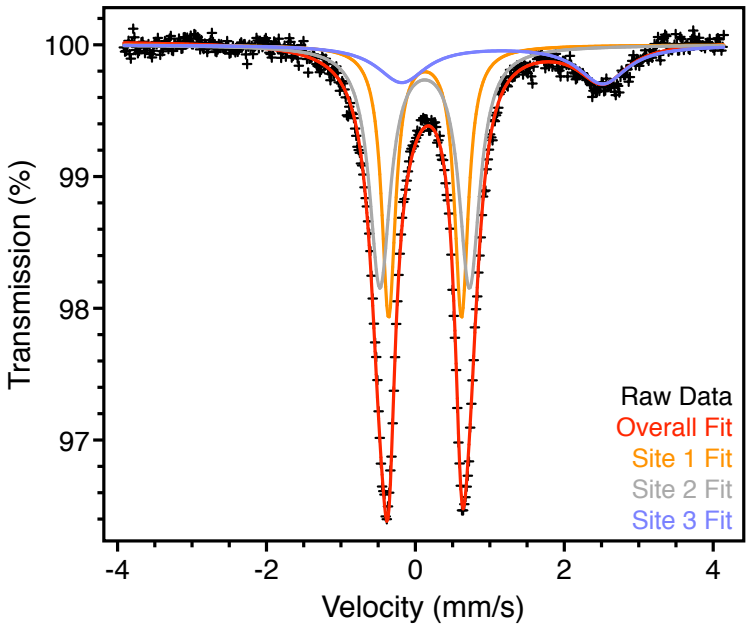

Figure S35. Mössbauer spectrum of $Mg_{0.85}Fe_2(bdp)_3$ collected at 5 K (black symbols) with overall fit (red curve), which consists of three distinct iron sites. Sites 1 and 2 correspond to low spin Fe^{III} sites, while site 3 corresponds to a high spin Fe^{II} site (Site 1: Area = 38%, δ = 0.13 mm/s, $|\Delta E_Q|$ = 0.98 mm/s , Γ = 0.23 mm/s; Site 2: Area = 47%, δ = 0.13 mm/s, $|\Delta E_Q|$ = 1.20 mm/s , Γ = 0.34 mm/s; Site 3: Area = 17%, δ = 1.17 mm/s, $|\Delta E_Q|$ = 2.70 mm/s, Γ = 0.81 mm/s). This spectrum is consistent with the expected level of framework reduction,[4] confirming Mg^{2+} is inserted into the framework pores.

References

1. H. J. Choi, M. Dinca and J. R. Long, *J. Am. Chem. Soc.*, 2008, **130**(25), 7848.
2. M. K. Taylor, T. e. Runčevski, J. Oktawiec, M. I. Gonzalez, R. L. Siegelman, J. A. Mason, J. Ye, C. M. Brown and J. R. Long, *J. Am. Chem. Soc.*, 2016, **138**(45), 15019.
3. Z. R. Herm, E. D. Bloch and J. R. Long, *Chem. Mater.*, 2013, **26**(1), 323.
4. M. L. Aubrey, B. M. Wiers, S. C. Andrews, T. Sakurai, S. E. Reyes-Lillo, S. M. Hamed, C.-J. Yu, L. E. Darago, J. A. Mason and J.-O. Baeg, *Nat. Mater.*, 2018, **17**(7), 625.
5. B. Bogdanović, K. Schlichte and U. Westeppe, *Chem. Ber.*, 1988, **121**(1), 27.
6. *SAINT, APEX2, and APEX3 Software for CCD Diffractometers*, Bruker Analytical X-ray Systems Inc., Madison, WI, USA, 2014.
7. G. M. Sheldrick, *SADABS*, Bruker Analytical X-ray Systems, Inc.: Madison, WI, 2014.
8. G. M. Sheldrick, *Acta Crystallographica Section A: Foundations and Advances*, 2015, **71**, 3-8.
9. G. M. Sheldrick, *Acta Crystallographica Section C: Structural Chemistry*, 2015, **71**, 3-8.
10. O. V. Dolomanov, L. J. Bourhis, R. J. Gildea, J. A. Howard and H. Puschmann, *J. Appl. Crystallogr.*, 2009, **42**(2), 339.
11. A. Coelho, *J. Appl. Crystallogr.*, 2003, **36**(1), 86.
12. A. Coelho, "TOPAS-Academic, version 4.1" 2007.

13. B. M. Wiers, PhD, UC Berkeley, 2015.
14. M. A. Spackman and D. Jayatilaka, *CrystEngComm*, 2009, **11**(1), 19.
15. M. J. Turner, J. J. McKinnon, S. K. Wolff, D. J. Grimwood, P. R. Spackman, D. Jayatilaka and M. A. Spackman, CrystalExplorer17 (2017). University of Western Australia. https://hirshfeldsurface.net.
16. J. J. McKinnon, D. Jayatilaka and M. A. Spackman, *ChemComm*, 2007, **37**, 3814.
17. I. Prisecaru, WMOSS4 Mössbauer Spectral Analysis Software, www.wmoss.org, 2009-2016.
18. Z. R. Herm, B. M. Wiers, J. A. Mason, J. M. van Baten, M. R. Hudson, P. Zajdel, C. M. Brown, N. Masciocchi, R. Krishna and J. R. Long, *Science*, 2013, **340**(6135), 960.
19. K. L. Mulfort, T. M. Wilson, M. R. Wasielewski and J. T. Hupp, *Langmuir*, 2008, **25**(1), 503.